



Extrinsic higher-order topological corner states in AB-stacked transition metal dichalcogenidesJiang Yao  and Linhu Li **Guangdong Provincial Key Laboratory of Quantum Metrology and Sensing & School of Physics and Astronomy, Sun Yat-Sen University (Zhuhai Campus), Zhuhai 519082, China*

(Received 12 August 2023; revised 9 November 2023; accepted 14 November 2023; published 12 December 2023)

Higher-order topological insulators are a novel type of topological phase that supports d -dimensional topological boundary states in D -dimensional systems with $D - d > 1$. In this work, we theoretically predict that interlayer couplings in AB-stacked bilayer transition metal dichalcogenides (TMDs) lead to the emergence of extrinsic second-order topological phases, where corner states are induced by the band inversion of zigzag edge bands. We find that the systems feature a quantized multiband Berry phase defined for a zigzag nanoribbon geometry, unveiling the nontrivial topological properties of its two zigzag edges. With a detailed investigation into the bilayer TMDs under different geometries, we find two types of boundary-obstructed corner states arising from different corner terminations of either the same type or heterogeneous zigzag edges. The topological nature of these corner states and their degeneracy is further analyzed with both the crystalline symmetries of different geometries and a topological phase transition of the Berry phase induced by layer-dependent on-site energy.

DOI: [10.1103/PhysRevB.108.245131](https://doi.org/10.1103/PhysRevB.108.245131)**I. INTRODUCTION**

Topological insulators are materials that exhibit robust boundary states, protected by a band gap and distinctive topological properties of their bulk states [1,2]. Their topological features can be classified into different “orders,” namely an n th-order topological insulator in d -dimension (dD) host topological boundary states in its $(d - n)D$ boundaries. Topological insulators with their orders of topology higher than 1 are known as higher-order topological insulators (HOTIs) [3,4]. Their realization has been proposed and implemented in both materials [5–9] and quantum simulation setups such as two-dimensional (2D) dielectric photonic crystals [10], acoustic crystals [11–14], and a two-dimensional continuous elastic system [15].

Over the past decade, exploring novel topological phases such as HOTIs in natural electronic systems has been one of the most active research topics in condensed-matter physics and material science [16–18]. Among the variety of natural materials, semiconducting 2D transition metal dichalcogenides (TMDs) possess a large bulk gap and in-gap 1D boundary states without dangling bonds [19–22], thus they provide an ideal platform for investigating various boundary phenomena. In particular, HOTI phases have been demonstrated to arise from double band inversion of surface states in the β - and γ -phases of TMDs [23], or from staggered coupling amplitudes between different orbitals and C_3 rotation symmetry in TMD monolayers [24–26], whose connection to the orbital Hall effect has been recently unveiled [27].

In this paper, we predict the presence of higher-order topological corner states in AB-stacked bilayer TMDs, based on a three-band tight-binding model describing the

low-energy and edge-state physics in monolayers of group-VIB TMDs [28]. Recently, such structures have been shown to support different types of first-order topological phases [29]. Conventionally, corner states are expected to be more accessible in TMDs with armchair boundaries, which possess a large energy gap between the 1D boundary states, while zigzag boundary states are gapless and may overwhelm possible corner states [19,24,25]. However, we find that interlayer couplings can induce a zigzag-boundary band inversion for bilayer TMDs, and they generate corner states corresponding to boundary obstructed topological phases with “extrinsic” higher-order topology, without relying on crystalline symmetries of the system [30–39]. Unlike a single monolayer, AB-stacking structure allows for two types of spatially symmetric zigzag boundaries, formed by boundaries of the two layers with different atoms. Interestingly, we find that different terminations between them give rise to two classes of corner states, where only one of them shows a direct correspondence to boundary-gap closing and a topological transition characterized by a Berry phase. These rich phenomena are exhaustively investigated with triangular, hexagonal, and parallelogram geometries, which support either one or both types of zigzag boundaries and thus different corner terminations.

The rest of this paper is organized as follows. In Sec. II, we introduce the three-orbital tight-binding model we use to describe AB-stacked bilayer TMDs, including their nontrivial topology characterized by a Berry phase, and crystalline symmetries that assist our analysis of corner states under different geometries. In Sec. III, we study the emergence of corner states and their behaviors during topological phase transitions of the Berry phase, in triangular, hexagonal, and parallelogram lattices, respectively, and we analyze their spatial configurations with the help of the presence and absence of different crystalline symmetries. A summary and some discussion of our results are given in Sec. IV.

*lilh56@mail.sysu.edu.cn

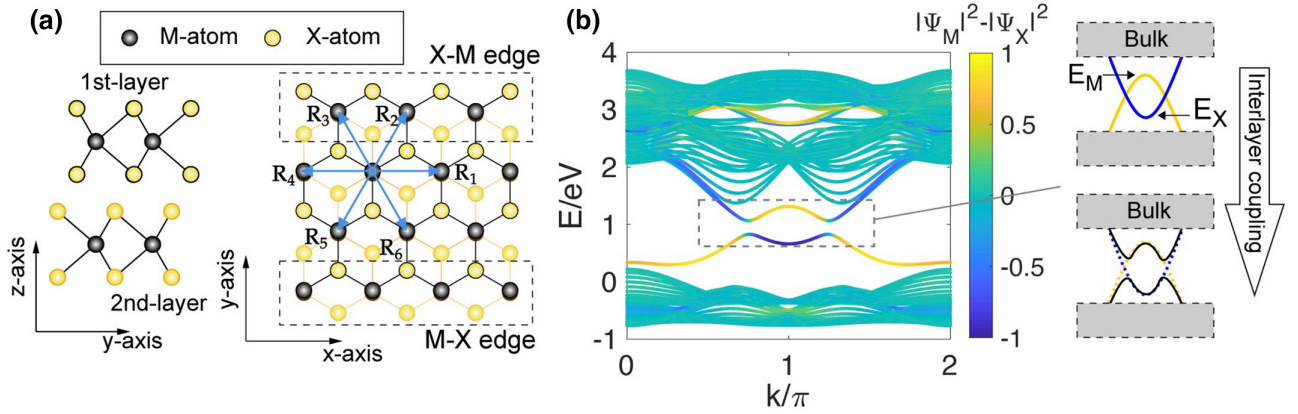


FIG. 1. Lattice structure and energy spectrum of AB-stacked bilayer TMDs. (a) Side view and top view of the model, with \mathbf{R}_1 to \mathbf{R}_6 indicating the nearest neighbors. Dashed boxes show different zigzag edges in AB-stacked TMDs. (b) Energy spectrum of a zigzag nanoribbon, with $\nu = 0.3$ eV and $\mu = 0$. Eigenstates are marked by different colors according to the quantity $|\Psi_M|^2 - |\Psi_X|^2$, where $|\Psi_M|^2$ ($|\Psi_X|^2$) is the sum distribution at M edges (X edges) of the two layers for each eigenstate, namely $|\Psi_M|^2 - |\Psi_X|^2 \approx 1$ for M edge states and ≈ -1 for X edge states. The right panel in (b) sketches the band inversion mechanism of zigzag edge bands. E_M and E_X are the maximal value of the M -edge band and the minimal value of the X -edge band, respectively. For MoS_2 , $E_M \approx 1.32$ eV and $E_X \approx 0.65$ eV.

II. MODEL

A. Lattice structure and Hamiltonian

The systems we consider are AB-stacked bilayer TMDs, commonly referred to as MX_2 , with M and X denoting atoms of transition metals and chalcogens, respectively, with a honeycomb-like structure as sketched in Fig. 1(a). To analyze the edge and corner physics, we adopt a three-orbital model for each layer [28], constructed using only the d_{z^2} , d_{xy} , and $d_{x^2-y^2}$ orbitals of M atoms, which gives a reasonable description of zigzag edge states of these materials, and it has been applied to investigate various edge phenomena therein [27,40–42]. The tight-binding Hamiltonian can be written as

$$\hat{H} = \hat{H}_{1\text{st}} + \hat{H}_{2\text{nd}} + \hat{H}_{\text{int}} + \frac{\mu}{2}(\hat{N}_1 - \hat{N}_2), \quad (1)$$

with $\hat{H}_{1\text{st}}$ ($\hat{H}_{2\text{nd}}$) the monolayer Hamiltonian for the top (bottom) layer, \hat{H}_{int} the interlayer couplings, and $\hat{N}_{1,2}$ the total electron number operator. The last term of μ describes the difference of on-site energy for the two layers, which may be induced by external electric fields applied perpendicular to the layers [43,44]. Note that a nonzero μ is not essential to induce corner states in our systems. However, it can lead to a topological phase transition that changes the number of corner states, as demonstrated in later sections.

Explicitly, the first two Hamiltonian operators are given by

$$\hat{H}_{1\text{st}} = \sum_{i,\mathbf{R}} \sum_{\alpha,\alpha'} \hat{a}_{i,\alpha}^\dagger t_{\mathbf{R},\alpha,\alpha'} \hat{a}_{i+\mathbf{R},\alpha'} + \sum_{i,\alpha} \hat{a}_{i,\alpha}^\dagger \epsilon_\alpha \hat{a}_{i,\alpha}, \quad (2)$$

$$\hat{H}_{2\text{nd}} = \sum_{i,\mathbf{R}} \sum_{\alpha,\alpha'} \hat{b}_{i,\alpha}^\dagger t_{\mathbf{R},\alpha,\alpha'} \hat{b}_{i+\mathbf{R},\alpha'} + \sum_{i,\alpha} \hat{b}_{i,\alpha}^\dagger \epsilon_\alpha \hat{b}_{i,\alpha}, \quad (3)$$

where $\hat{a}_{i,\alpha}^\dagger$ ($\hat{b}_{i,\alpha}^\dagger$) creates an electron at lattice site i and orbital α in the top (bottom) layer, \mathbf{R} is one of the six vectors connecting nearest-neighbor M atoms, with $t_{\mathbf{R},\alpha,\alpha'}$ being its corresponding hopping strength [see Fig. 1(a) and Table I], and ϵ_α are on-site energies corresponding to different orbitals.

The third term \hat{H}_{int} in Eq. (1) is the interlayer hopping. Using a Slater-Koster table [45], \hat{H}_{int} reads

$$\begin{aligned} \hat{H}_{\text{int}} = & \hat{a}_{i,d_{z^2}}^\dagger V_{dd\sigma} \hat{b}_{i,d_{z^2}} + \hat{a}_{i,d_{xy}}^\dagger V_{dd\delta} \hat{b}_{i,d_{xy}} \\ & + \hat{a}_{i,d_{x^2-y^2}}^\dagger V_{dd\delta} \hat{b}_{i,d_{x^2-y^2}} + \text{H.c.}, \end{aligned} \quad (4)$$

where $V_{dd\sigma}$ and $V_{dd\delta}$ are two types of overlap integrals of different d - d orbitals, and $V_{dd\sigma}$ is generally much larger than $V_{dd\delta}$ for a relatively large distance between M atoms [46,47]. In the following discussion, we shall assume

$$V_{dd\sigma} = \nu, \quad V_{dd\delta} = 0.3\nu, \quad (5)$$

and we use the tight-binding parameters for MoS_2 given in Ref. [28] ($\epsilon_{d_{z^2}} = 1.046$ eV, $\epsilon_{d_{xy}} = \epsilon_{d_{x^2-y^2}} = 2.104$ eV; see Table I for other parameters), unless otherwise specified.

B. Zigzag edge states and edge-band inversion in a nanoribbon structure

To reveal the topological nature that gives rise to higher-order corner states, we take a look at the system with a zigzag nanoribbon structure along the x direction. When $\mu = \nu = 0$, our model reduces to two identical monolayers of TMDs, where edge bands of different zigzag edge states (namely, M -edge and X -edge) of the two layers cross each other in their eigenenergies. The AB-stacked structure allows for a mixture of the two branches of edge states on the same edge of the bilayer TMD, denoted as M - X or X - M edge according to the boundary atoms of the two layers [see Fig. 1(a)]. Thus, with a nonzero ν that couples M - and X -edges of different layers, an edge-band inversion occurs and opens a boundary gap between these edge states, as shown in Figs. 1(b) and 1(c). Note that these edge states are twofold-degenerate when $\mu = 0$, due to an inversion symmetry between M - X and X - M edges. With a nonzero μ , the degeneracy is lifted, and one pair of edge states is separated in energy (the one at X - M edge for a positive μ), resulting in a reversed process of band inversion and thus a topological phase transition, as shown

TABLE I. Hopping amplitudes $t_{R,\alpha,\alpha'}$ for TMDs [28,40]. Different rows show hoppings between different orbitals, and different columns are for different spatial hopping vectors \mathbf{R} for the top layer in Fig. 1(a). For the bottom layer, $\mathbf{R}_1, \mathbf{R}_2$, and \mathbf{R}_3 are exchanged with $\mathbf{R}_4, \mathbf{R}_5$, and \mathbf{R}_6 , respectively. For MoS₂, the parameters are approximately given by $t_0 = -0.184, t_1 = 0.401, t_2 = 0.507, t_{11} = 0.218, t_{12} = 0.338$, and $t_{22} = 0.057$ (in eV) [40].

$\alpha-\alpha'$	\mathbf{R}_1	\mathbf{R}_2	\mathbf{R}_3	\mathbf{R}_4	\mathbf{R}_5	\mathbf{R}_6
$d_{z^2}-d_{z^2}$	t_0	t_0	t_0	t_0	t_0	t_0
$d_{xy}-d_{xy}$	t_{11}	$\frac{t_{11}+3t_{22}}{4}$	$\frac{t_{11}+3t_{22}}{4}$	t_{11}	$\frac{t_{11}+3t_{22}}{4}$	$\frac{t_{11}+3t_{22}}{4}$
$d_{x^2-y^2}-d_{x^2-y^2}$	t_{22}	$\frac{3t_{11}+t_{22}}{4}$	$\frac{3t_{11}+t_{22}}{4}$	t_{22}	$\frac{3t_{11}+t_{22}}{4}$	$\frac{3t_{11}+t_{22}}{4}$
$d_{z^2}-d_{xy}$	t_1	$\frac{t_1+\sqrt{3}t_2}{2}$	$-\frac{t_1+\sqrt{3}t_2}{2}$	$-t_1$	$-\frac{t_1-\sqrt{3}t_2}{2}$	$\frac{t_1-\sqrt{3}t_2}{2}$
$d_{z^2}-d_{x^2-y^2}$	t_2	$-\frac{t_2-\sqrt{3}t_1}{2}$	$-\frac{t_2-\sqrt{3}t_1}{2}$	t_2	$-\frac{t_2+\sqrt{3}t_1}{2}$	$-\frac{t_2+\sqrt{3}t_1}{2}$
$d_{xy}-d_{x^2-y^2}$	t_{12}	$\frac{\sqrt{3}(t_{11}-t_{22})}{4} - t_{12}$	$\frac{\sqrt{3}(t_{22}-t_{11})}{4} + t_{12}$	$-t_{12}$	$\frac{\sqrt{3}(t_{11}-t_{22})}{4} + t_{12}$	$\frac{\sqrt{3}(t_{22}-t_{11})}{4} - t_{12}$

in Fig. 2. These different topological phases can be further characterized by a multiband Berry phase γ , defined as

$$\gamma = -i \sum_l \log \det U(k_l), \quad (6)$$

where $U_{mn}(k_l) = \langle \psi_m(k_l) | \psi_n(k_{l+1}) \rangle$ is the (m, n) element of the link matrix $U(k_l)$, $|\psi_m(k_l)\rangle$ is the Bloch wave function of the m th band at the discrete crystal momentum k_l , and $m, n \in [1, N_{\text{occ}}]$, with N_{occ} the number of occupied bands (all bands below the edge-gap in our case; see Fig. 2).

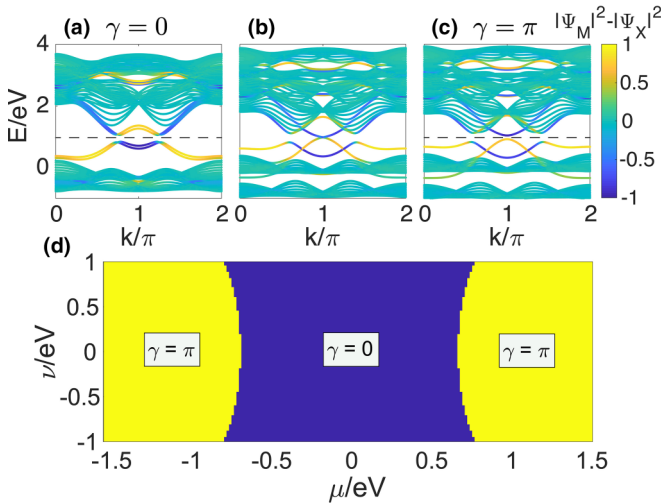


FIG. 2. Energy spectrum and a topological phase diagram of the bilayer TMDs in a nanoribbon structure, with $\mu = 0.1, 0.68$, and 0.8 eV from (a) to (c), respectively, and the same colormap as in Fig. 1(b), indicating distribution of each eigenstate at M and X edges. With increasing μ , a reversed process of band inversion occurs for one pair of edge states, which becomes topologically trivial after the transition at $\mu \approx 0.67$ eV. In (a) and (c), γ is calculated for all eigenstates below the band gap (indicated by the dashed lines). We find $\gamma = 0$ in (a) as edge-band inversion occurs for both M - X and X - M edge states, which possess the opposite single-band Berry phase (see Appendix A). In (c), we have $\gamma = \pi$ since one pair of these edge states is trivialized after the topological phase transition. 1D edge states in (b) are gapless, and thus the Berry phase is ill-defined. Other parameters are the same as in Fig. 1(b). (d) A phase diagram determined by the value of γ .

Numerically, we find that $\gamma = 0$ for small μ with band inversion for both M - X and X - M edge states [Fig. 2(a)], as they possess opposite topological charges characterized by edge-band Berry phases of $\pm\pi$, respectively (see Appendix A). Nonetheless, corner states may still emerge under the full OBCs with different geometries, as demonstrated in later sections. This is because the 1D edges are spatially separated by the bulk, therefore their opposite topological charges cannot annihilate each other. On the other hand, increasing μ will lead to a topological phase transition and trivialize one pair of edge states, resulting in a π Berry phase contributed solely by the other pair with edge-band inversion, as illustrated in Fig. 2(c). Following this analysis, the topological phase transition shall occur when the amplitude of μ matches the energy difference between the maximal value of M -edge band and the minimal value of X -edge band [see Fig. 1(b)], $\mu \approx |E_M - E_X| \approx 0.67$ eV, which is verified in the explicit examples discussed in later sections. A topological phase diagram regarding different values of ν and μ is displayed in Fig. 2(d), which shows that the strength of interlayer coupling ν does not affect much the Berry phase or the topological transition induced by μ . In other words, the nontrivial topology and its corresponding higher-order corner states are not sensitive to the exact value of interlayer couplings, and thus can be expected to manifest in a more realistic parameter regime [compared with our assumption in Eq. (5)] of TMD materials.

C. Crystalline symmetries of the AB-stacked bilayer TMDs

Although not essential to the extrinsic higher-order corner states, the lattice structure of TMDs naturally hosts several crystal symmetries, which are useful in our analysis of corner states under different geometries. In particular, the space symmetry group of monolayer TMDs is the D_{3h} point group, containing symmetry operators $\{\hat{E}, \hat{C}_3, \hat{C}_3^2, \hat{M}_x, \hat{M}_1, \hat{M}_2\}$, where \hat{E} is the identity operation, \hat{C}_3 is the rotation by $\frac{2\pi}{3}$ about the z -axis, \hat{M}_x is the mirror-reflection along the x -axis, and \hat{M}_1 and \hat{M}_2 are obtained through rotating \hat{M}_x around the z -axis by $\frac{2\pi}{3}$ and $\frac{4\pi}{3}$, respectively. In addition to these symmetries, AB-stacked bilayer TMDs (without a boundary) further satisfy a 3D inversion symmetry described by the operator $\hat{I} = \sigma_x \hat{R}$, with σ_x exchanging the two layers, and \hat{R} is the central rotation around the z -axis of 180° . An extra

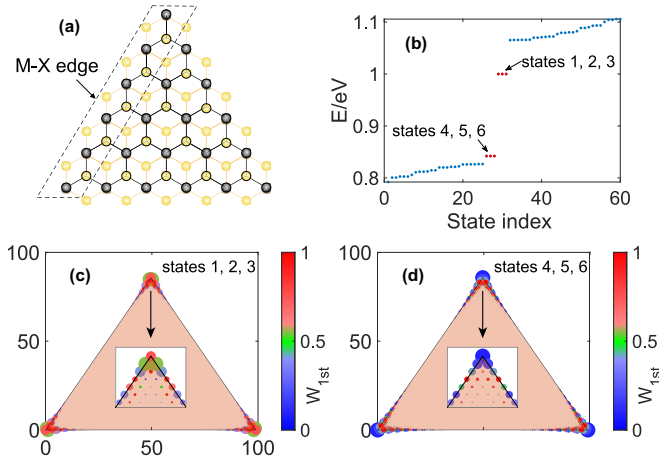


FIG. 3. Lattice structure and corner states in AB-stacked bilayer TMDs with a triangular structure. (a) Top view of the triangular lattice. (b) A total of 60 eigenenergies close to $E = 0.95$ eV, with two sets of threefold-degenerate corner states (red) within the energy gap. (c),(d) Distribution of the two sets of threefold-degenerate corner states, respectively. The size of each point is proportional to the summed distribution at each site i , $\rho_i = \sum_{\alpha,n} (|\psi_{i,\alpha,n}^{1st}|^2 + |\psi_{i,\alpha,n}^{2nd}|^2)$, with α denoting the three orbitals and n summing over the three states indicated in each panel. The colormap displays the value of W_i^{1st} , the weight of occupation on the first layer for each site. Namely, $W_i^{1st} = 1$ (0) means that the states occupy only the first (second) layer on the lattice site indexed by i . The system's size is chosen to have 100 M atoms along each edge. Other parameters are $\nu = 0.3$ eV and $\mu = 0$.

interlayer-mirror symmetry along the y -axis also emerges, described by the operator $\hat{M}'_y = \hat{I}\hat{M}_x$, which represents a combination of mirror-reflection along the y -axis and exchanging the two layers. This symmetry is also equivalent to a C_2 symmetry around the x axis in 3D.

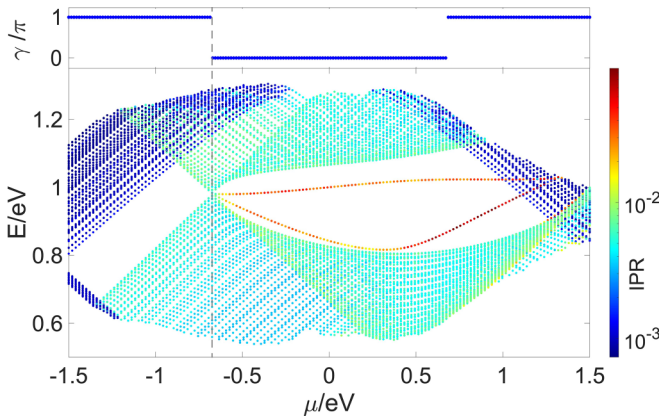


FIG. 4. Energy spectrum and Berry phase γ vs the layer-dependent on-site energy μ , for the triangular lattice with M - X edges and $\nu = 0.3$ eV. A total of 200 energy points around $E = 0.92$ eV are taken in our numerics. The side length of the lattice is chosen to be 70 M atoms. The energy spectrum for the triangular lattice with X - M edges is identical to the current one by changing μ to $-\mu$, as the two types of edges can be mapped to each other through the inversion operation.

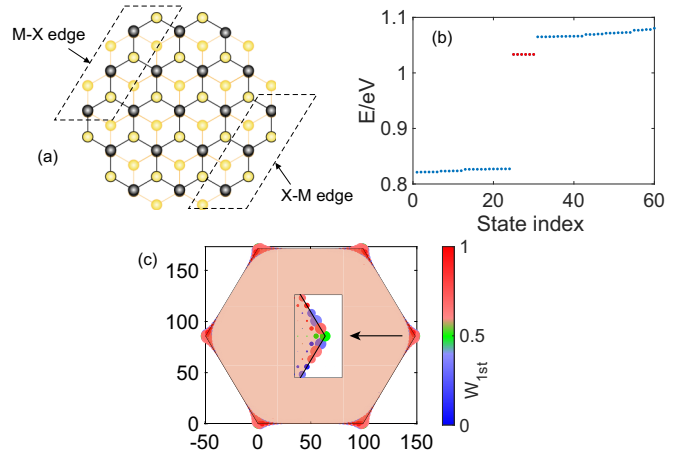


FIG. 5. Lattice structure and corner states in AB-stacked bilayer TMDs with a hexagonal structure. (a) Top view of the hexagonal lattice. (b) A total of 60 eigenenergies close to $E = 0.95$ eV, with a set of sixfold-degenerate corner states (red) within the energy gap. (c) Distribution of the six degenerate corner states. The size of each point is proportional to the summed distribution ρ_i at site i , and the colormap displays the value of W_i^{1st} . The system's size is chosen to have 100 M atoms along each edge. Other parameters are $\nu = 0.3$ eV and $\mu = 0$.

III. CORNER STATES UNDER DIFFERENT GEOMETRIC STRUCTURES

As seen in Fig. 2, nontrivial topological properties in our model originate from an edge-band inversion, which shall lead to the emergence of boundary obstructed topological corner states in the edge-gap near $E = 0.95$ eV (dashed lines in Fig. 2) under the full OBCs. More intriguingly, these corner states may show distinguished behaviors depending on the geometry of an OBC lattice, since shearing the lattice along different directions will result in junctions either between heterogeneous M - X and X - M edges, or two edges of the same type.

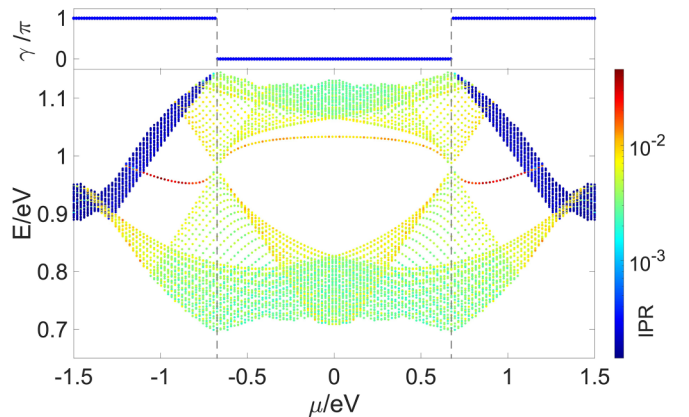


FIG. 6. Energy spectrum and Berry phase γ vs the layer-dependent on-site energy μ , for the hexagonal lattice with $\nu = 0.3$ eV. A total of 200 energy points around $E = 0.92$ eV are taken. The side length of the lattice is chosen to be 70 M atoms.

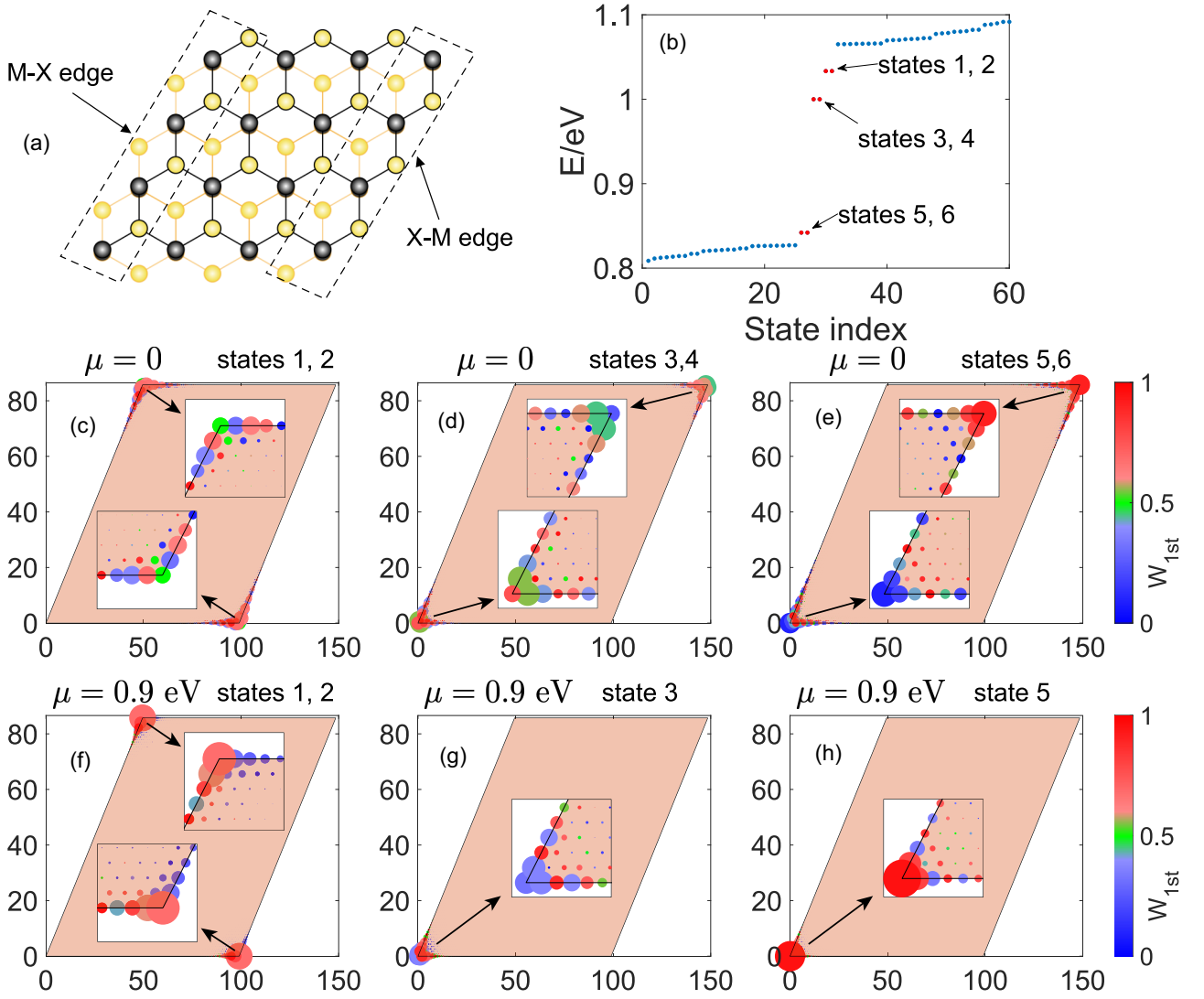


FIG. 7. Lattice structure and corner states in AB-stacked bilayer TMDs with a parallelogram structure. (a) Top view of the parallelogram lattice. (b) A total of 60 eigenenergies close to $E = 0.95$ eV at $\mu = 0$, with three sets of twofold-degenerate corner states (red) within the energy gap. (c)–(e) Distribution of the three sets of degenerate corner states, respectively, with $\mu = 0$. The size of each point is proportional to the summed distribution ρ_i at site i , and the colormap displays the value of W_i^{1st} . The system's size is chosen to have $N_x = N_y = 100$, with N_x and N_y the number of M atoms along x and y directions, respectively. (f) Distribution of the degenerate corner states (1,2) with $\mu = 0.9$ eV. (g),(h) Distribution of a single nondegenerate corner state with $\mu = 0.9$. These two states are marked as states 3 and 5, as they correspond to states (3,4) and (5,6) in a different topological phase with $|\mu| \lesssim 0.67$ eV (see Fig. 8). $\nu = 0.3$ eV is chosen for all panels.

A. Triangular structure

We first consider AB-stacked bilayer TMDs with a triangular geometry, as shown in Fig. 3(a). A triangular lattice has three equivalent boundaries of the same type, and here we take the case with M - X edges as an example. In addition, it satisfies the threefold rotation symmetry of \hat{C}_3 , but not the inversion symmetry that exchanges the two layers. Thus the corner states in a triangular bilayer TMD are expected to be symmetric between different corners, and asymmetric between the two layers.

In Fig. 3(b), we display our numerical results of eigenenergies for the triangular structure. Two sets of threefold-degenerate states with different energies are found within the edge gap. Note that the energies (and those in later examples) of these corner states are generally nonzero, due to the lack

of protection from global discrete symmetries (e.g., chiral symmetry or charge-conjugation symmetry) [3]. Their distributions in real space are shown in Figs. 3(c) and 3(d), where each set of degenerate states is distributed symmetrically on the three corners. On the other hand, the two sets of corner states exhibit different occupation on the two layers, as can be seen from the weight of occupation on each site of the first layer,

$$W_i^{1st} = \sum_{n,\alpha} |\psi_{i,\alpha,n}^{1st}|^2 / \left(\sum_{n,\alpha} |\psi_{i,\alpha,n}^{1st}|^2 + \sum_{n,\alpha} |\psi_{i,\alpha,n}^{2nd}|^2 \right), \quad (7)$$

with $\psi_{i,\alpha,n}^{1st(2nd)}$ the amplitude at the i th site of the first (second) layer of an eigenstate indexed by n , and the summation runs over all orbitals (indexed by α) for a set of degenerate corner

states. Namely, states 1, 2, and 3 show a roughly balanced occupation on the two layers, and states 4, 5, and 6 mostly occupy the second layer. Such asymmetric layer occupation for corner states at different eigenenergies reflects the absence of the inversion symmetry of $\hat{I} = \sigma_x \hat{R}$ in the triangular lattice.

In Fig. 4, we illustrate the eigenenergies around the energy gap as a function of the layer-dependent on-site energy μ , which are marked by different colors according to the inverse participation ratio (IPR) of their eigenstates, defined as

$$\text{IPR}(n) = \sum_i \left[\sum_{\alpha} (|\psi_{i,\alpha,n}^{\text{1st}}|^2 + |\psi_{i,\alpha,n}^{\text{2nd}}|^2) \right]^2. \quad (8)$$

As can be seen from the figure, by turning on the layer-dependent on-site energy μ , the energy gap closes between 1D edge states at $\mu \approx -0.67$ eV, and corner states disappear when further decreasing the (negative) value of μ . Such an observation matches a jump of the Berry phase γ from 0 to π , yet with two unconventional properties seemingly contradictory to conventional bulk-boundary correspondence of topological phases: (i) corner states emerge with a trivial Berry phase ($\gamma = 0$), and they disappear with a nontrivial one ($\gamma = \pi$); and (ii) the same edge-gap closing does not occur at the other topological transition point of $\mu \approx 0.67$ eV.

To understand these enigmatic behaviors, we note that the Berry phase is calculated under the nanoribbon geometry with both M - X and X - M edges, and the “trivial” phase with $\gamma = 0$ is in fact nontrivial with single-band Berry phases of $\pm\pi$ for the two edge bands, as discussed for Fig. 2 and in Appendix A. The triangular lattice we consider in Fig. 3 possesses only M - X edges, therefore it only inherits “half” of the topological properties of a nanoribbon geometry, which is trivialized when $\mu \lesssim -0.67$ eV. Alternatively, a triangular lattice with X - M edges shall inherit the other “half” of the topological properties, possessing a spectrum symmetric to Fig. 4 regarding $\mu = 0$, with a topological phase transition at $\mu \approx 0.67$ eV (not shown). As a side note, a large amplitude of μ will shift different bulk bands of the two layers and mix them in energy, thus all corner states will eventually merge into the bulk bands even without a topological transition, as seen in Fig. 4 with $\mu \gtrsim 1$ eV.

B. Hexagonal structure

Next we consider a hexagonal structure of the AB-stacked bilayer TMDs, as sketched in Fig. 5(a). Unlike the triangular lattice, a hexagonal lattice has adjacent M - X and X - M edges, and satisfies both the inversion symmetry of $\hat{I} = \sigma_x \hat{R}$ and the threefold rotation symmetry of \hat{C}_3 . Consequently, corner states in the hexagonal lattice shall be sixfold-degenerate, and distribute evenly on the two layers, as verified by our numerical results in Figs. 5(b) and 5(c).

Due to the different boundary terminations, corner states of the hexagonal lattice behave rather differently across the topological phase transition characterized by the Berry phase γ . As demonstrated in Fig. 6, the sixfold-degenerate corner states survive in all three parameter regions separated by the gap closing at $\mu \approx \pm 0.67$ eV (except that they merge into bulk bands for $\mu \gtrsim 1$ eV). This is because under a hexagonal geometry, each corner connects two distinct M - X and X - M

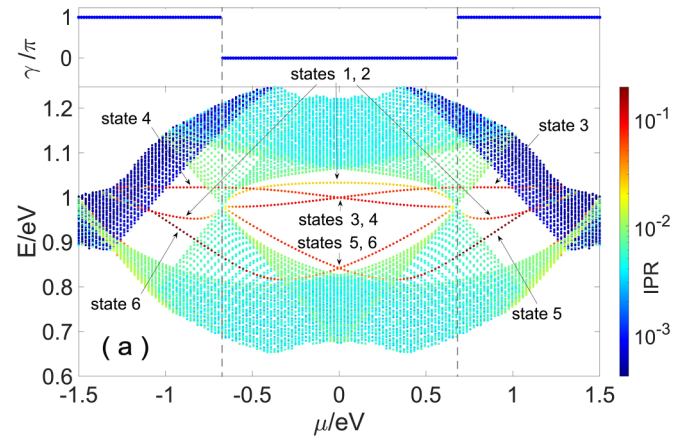


FIG. 8. Energy spectrum and Berry phase γ vs the layer-dependent on-site energy μ , for the parallelogram lattice with $v = 0.3$ eV. A total of 200 energy points around $E = 0.92$ eV are taken. The size of the lattice is chosen to be $N_x = N_y = 70$.

edges, and at least one of them is governed by nontrivial topology in the three parameter regions, resulting in a corner state at each of their joint corners.

C. Parallelogram structure

From the aspect of boundary terminations, a parallelogram structure can be viewed as a mixture of triangular and hexagonal ones, as it support both types of corners connecting either the same or two different M - X and X - M edges, as sketched in Fig. 7(a). Consequently, corner states in a parallelogram lattice are expected to behave differently on different types of corners, which is also suggested by the lack of C_3 rotation symmetry in such a geometry.

The energy spectrum around the zigzag edge gap of AB-stacked bilayer TMDs in a parallelogram geometry is shown in Fig. 7(b), where three sets of twofold-degenerate corner states are found inside the gap. Their distribution in real space is illustrated in Figs. 7(c)–7(e), where one set of corner states (labeled as states 1 and 2) occupies the top-left and bottom-right corners, in analogy to the corner states in the hexagonal lattice, and the remaining two sets (labeled as states 3–6) occupy the other two corners, in analogy to the corner states in the triangular lattice. Remarkably, due to the presence of inversion symmetry ($\hat{I} = \hat{R}\sigma_x$), each set of corner states now exhibits a symmetric distribution on the two layers, in contrast to the case of the inversion-asymmetric triangular lattice.

Due to their different boundary terminations, these corner states behave rather differently upon turning on a nonzero μ . As demonstrated in Fig. 8, the hexagon-analogous corner states (1,2) remain degenerate and exist for all values of μ , as they both originate from the same type of joint corners between M - X and X - M edges. In contrast, the two triangle-analogous corner states of a degenerate pair [(3,4) or (5,6)] originate from corners of different types of edges. That is, the bottom-left corner connects two M - X edges, and the top-right corner connects two X - M edges. As discussed previously for the triangular lattice, these two types of corners react to μ differently (but symmetric about $\mu = 0$), therefore their degeneracy is lifted by a nonzero μ . Further increasing

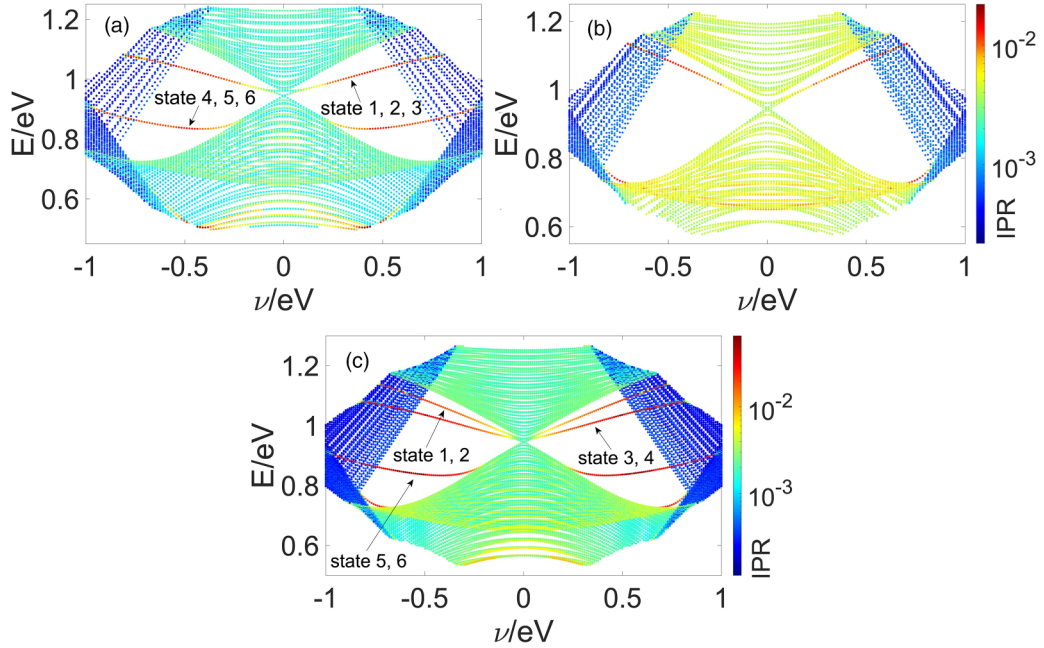


FIG. 9. Energy spectrum at $\mu = 0$ vs interlayer hopping strength ν for (a) the triangular structure with 200 points around 0.87 eV, (b) the hexagonal structure with 300 points around 0.9 eV, and (c) the parallelogram structure with 200 points around 0.9 eV.

the amplitude of μ , a topological phase transition occurs for the M - X (X - M) edge when $\mu < 0$ ($\mu > 0$), and one corner state of each triangle-analogous pair disappears when $|\mu| \gtrsim 0.67$ eV. The disappearance of two corner states at the same corner is in agreement with our results and analysis for the triangular lattice, which hosts three C_3 -rotation-symmetric corners connecting the same type of edges. In Fig. 9, we display the energy spectra versus ν under different geometries. It is seen that corner states of the triangular lattice in Fig. 9(a) [the hexagonal lattice in Fig. 9(b)] match well with corner states 3–6 (1 and 2) of the parallelogram lattice in Fig. 9(c), which further verifies the analogy between these corner states.

The above observations and analysis imply that in the parallelogram lattice, the twofold degeneracy of triangle-analogous corner states is protected by the inversion symmetry. A nonzero μ breaks the symmetry and lifts this degeneracy. On the other hand, the threefold degeneracy of corner states in the triangular lattice is protected by the C_3 rotational symmetry, which is not affected by μ . Similarly, the twofold degeneracy of hexagon-analogous corner states in the parallelogram lattice, and the sixfold degeneracy of corner states in the hexagonal lattice, are also protected by different crystal symmetries and/or the conditions of corner terminations. Nevertheless, despite these different symmetry protections of degeneracy, we argue that the emergence of these corner states can still be attributed to the topological properties associated with the multiband and edge-band Berry phases, as analyzed throughout this paper, and summarized in Table II.

IV. SUMMARY AND DISCUSSION

We have unveiled a class of extrinsic higher-order topological phases induced by interlayer couplings in AB-stacked

bilayer TMDs, which host corner states insensitive to crystal symmetries of the materials. Explicitly, the zigzag edge states of these materials cross each other in their eigenenergy, thus a band inversion between them can be induced by nonzero interlayer couplings, leading to gapped edge bands and the emergence of in-gap corner states. The relatively large edge-band crossing region in energy indicates the robustness of these corner states against possible disorders or perturbations. With exhaustive investigation into the system with different triangular, hexagonal, and parallelogram geometries, we uncover two types of corner states corresponding to different corner terminations between the M - X and X - M zigzag edges for the bilayer structure. The topological nature of these corner states is justified by a multiband Berry phase defined for the system in a nanoribbon geometry, which reflects the overall topological properties of both types of zigzag edges. Topological phase transitions of the system induced by an on-site energy detuning μ of the two layers are studied accordingly. We find that the M - X and X - M edges can be trivialized only for negative and positive μ ,

TABLE II. Relation between the corner states and Berry phases. γ_{MX} and γ_{XM} are the Berry phases for the corresponding edge bands (see Appendix A). Numbers in the last three columns indicate the numbers of corner states and their degeneracy. For example, 2/1/1 means that there are a pair of twofold-degenerate corner states, and two nondegenerate corner states.

γ	μ	Edge topology		Corner states under different geometries		
		γ_{MX}	γ_{XM}	M - X (X - M)	\triangle	\square
0	\pm	π	π	3/3	6	2/1/1/1/1
π	+	π	0	3/3 (0)	6	2/1/1
π	-	0	π	0 (3/3)	6	2/1/1

respectively, leading to distinct behaviors for the two types of corner states when a topological phase transition occurs. Our results show that the higher-order corner states in bilayer TMDs are highly tunable due to the abundant bilayer structures and layer-dependent physical effects (such as a perpendicular electric field), and thus hold great promise for quantum applications. On the other hand, these corner states are also stable against boundary perturbations, as shown in Appendix D.

Throughout our study, we have focused only on the zigzag edges, as they support gapless edge states and thus an edge band inversion can be induced by weak interlayer couplings. In Appendix B, we have further demonstrated numerical results of the AB-stacked bilayer TMDs in a square lattice, which support both zigzag and armchair edges. We find that corner states in square lattices may be attributed to either zigzag- or armchair-edge band inversion, yet the latter occurs only with a relatively large interlayer hopping strength, due to the large armchair-edge band gap of monolayer TMDs.

ACKNOWLEDGMENT

This work is supported by the Guangdong Project (Grant No. 2021QN02X073).

APPENDIX A: SINGLE-BAND BERRY PHASES

In this Appendix, we discuss the properties of single-band Berry phase γ_n for the zigzag edges of AB-stacked bilayer TMDs. It follows a similar definition to Eq. (6) in the main

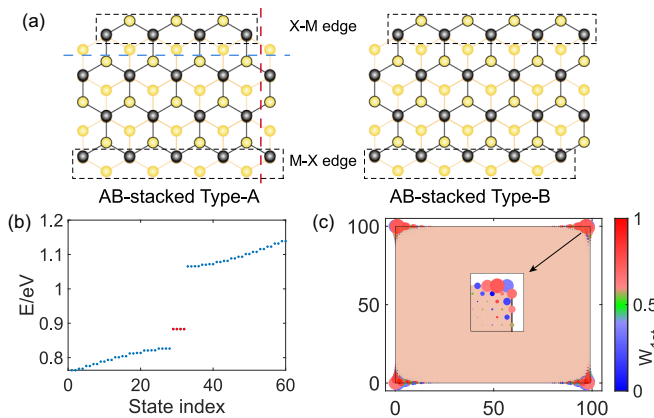


FIG. 10. Lattice structure and corner states in AB-stacked bilayer TMDs with square structures. (a) Top view of different types of square structures. A type-B lattice can be obtained from a type-A one by shearing along the red dashed line. Shearing along the blue dashed line changes the parity of N_y . (b) A total of 60 eigenenergies close to $E = 0.95$ eV at $\mu = 0$ for the type-A square lattice with an odd N_y , with four degenerate corner states (red) within the energy gap. (c) Distribution of the degenerate corner states, where the size of each point is proportional to the summed distribution ρ_i at site i , and the colormap displays W_i^{1st} , the weight of the first-layer occupation on each site. The system's size is chosen to be $N_x = 100$ and $N_y = 101$. Other parameters are $\mu = 0$ and $\nu = 0.3$ eV.

TABLE III. Symmetry table for different types of AB-stacked bilayer TMDs with square structure. N_y is the number of M atoms along the y -direction.

	Type A	Type B
N_y is odd ($N_y > 1$)	$\{\hat{E}, \hat{M}_x, \hat{I}, \hat{M}'_y\}$	$\{\hat{E}, \hat{M}'_y\}$
N_y is even	$\{\hat{E}, \hat{M}_x\}$	$\{\hat{E}, \hat{I}\}$

text,

$$\gamma_n = -i \sum_l \log U_n(k_l), \quad (\text{A1})$$

with $U_n(k_l) = \langle \psi_n(k_l) | \psi_n(k_{l+1}) \rangle$ and $\langle \psi_n(k_l) \rangle$ the Bloch wave function of the n th band at the discrete crystal momentum k_l . Here we consider the two degenerate edge bands belong the energy gap in Fig. 1(b), labeled as ψ_{MX} and ψ_{XM} , respectively, regarding their occupied edges. Due to the presence of inversion symmetry, these two edge bands are symmetric to each other between k and $-k$, i.e.,

$$\hat{I}_y |\psi_{MX}(k)\rangle = |\psi_{XM}(-k)\rangle,$$

with $\hat{I}_y = \hat{M}_y \sigma_x$ the inversion operation in the y - z plane (the same as \hat{M}'_y discussed in Sec. II C). In addition, the model also satisfies the time-reversal symmetry $\hat{H}(k) = \hat{H}^*(-k)$, or $|\psi(k)\rangle = |\psi^*(-k)\rangle$ for eigenstates. Thus the link variable $U_n(k)$ for these two bands satisfies

$$\begin{aligned} U_{MX}(k) &= \langle \psi_{MX}(k_l) | \psi_{MX}(k_{l+1}) \rangle \\ &= \langle \psi_{XM}(-k_l) | \psi_{XM}(-k_{l+1}) \rangle \\ &= \langle \psi_{XM}(k_l)^* | \psi_{XM}(k_{l+1})^* \rangle \\ &= \langle \psi_{XM}(k_l) | \psi_{XM}(k_{l+1}) \rangle^* \\ &= U_{XM}(k)^*, \end{aligned} \quad (\text{A2})$$

which leads to $\gamma_{MX} = -\gamma_{XM}$. Therefore, the Berry phase of two boundary states vanishes at on-site energy $\mu = 0$.

Although these edge-band Berry phases are obtained for $\mu = 0$, their symmetric behavior is expected to hold even when the inversion symmetry is broken by a nonzero μ , unless a topological phase transition occurs for one of the two edge bands. However, these edge-band Berry phases may be ill-defined when the amplitude of μ increases, since the corresponding edge bands may partially merge into the valence bulk bands [e.g., see Figs. 2(b) and 2(c) in the main text]. Therefore, we have only considered the multiband Berry phase γ in most of the main text. Nevertheless, in most of the parameter region we consider (including the topological transition point), there is at most one edge band merging into the bulk. Hence we can calculate the (well-defined) Berry phase for the other isolated edge band, and obtain the ill-defined one through $\gamma = \gamma_{XM} + \gamma_{MX}$, since bulk bands never close their energy gap and are always topologically trivial in our considered cases.

APPENDIX B: CORNER STATES OF SQUARE STRUCTURE

In this Appendix, we discussed AB-stacked TMDs with square structure, which host both armchair and zigzag edges. Taking into account two types of M - X and X - M zigzag edges,

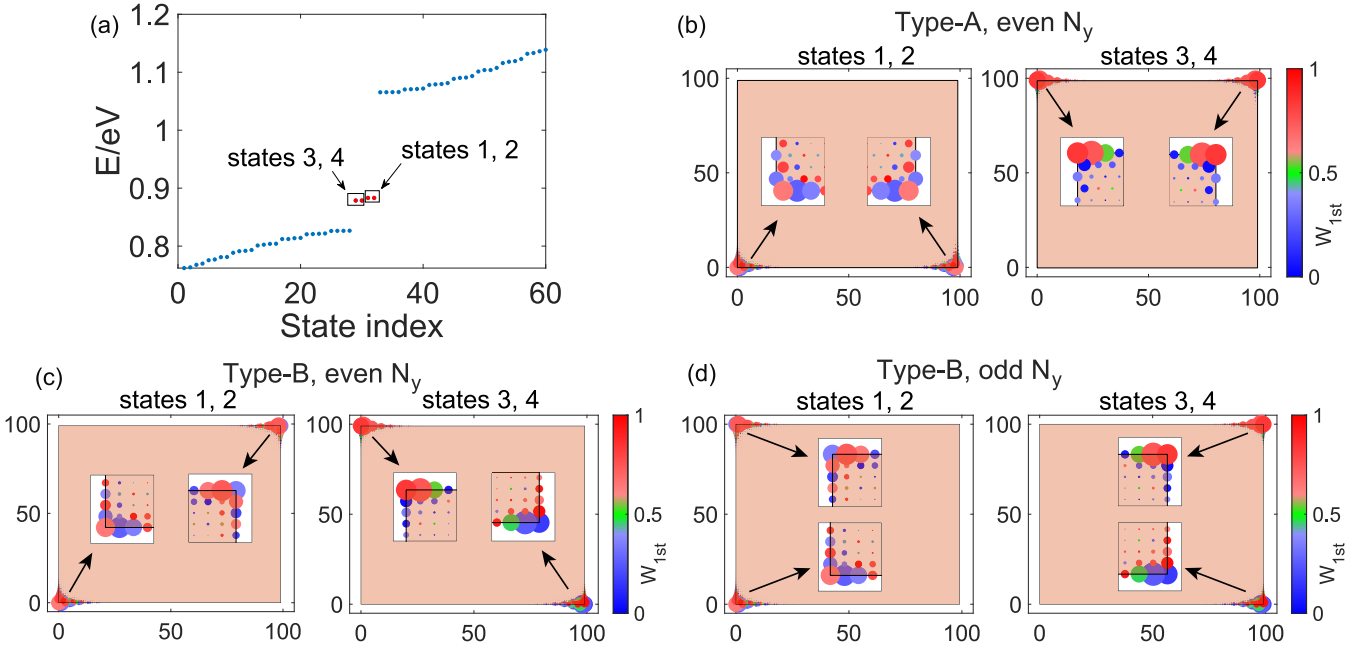


FIG. 11. Spectrum and corner states for different types of square lattices. (a) A total of 60 eigenenergies close to $E = 0.95$ eV at $\mu = 0$ for the type-A square lattice with an even N_y , with two sets of twofold-degenerate corner states (red) within the energy gap. Spectra for type-B square lattices (for both even and odd N_y) are qualitatively the same as (a). (b)–(d) Distribution of the the degenerate corner states for type-A with even N_y ($N_x = 100, N_y = 100$), type-B with even N_y ($N_x = 100, N_y = 100$), and type-B with odd N_y ($N_x = 100, N_y = 101$), respectively. The size of each point is proportional to the summed distribution ρ_i at site i , and the colormap displays W_{i}^{1st} , the weight of the first-layer occupation on each site. Other parameters are $\mu = 0$ and $\nu = 0.3$ eV.

we obtain four types of different nanoflakes, namely type-A and type-B denoted in Fig. 10(a), with either an even or an odd N_y , the number of M atoms along the y direction. Their corresponding symmetries are indicated in Table III.

As seen in Figs. 10(b) and 10(c), a type-A square lattice with an odd N_y has four degenerate corner states, distributing evenly on the four corners. This is because it is the most symmetric case in the four types of square lattices, satisfying both the inversion symmetry \hat{I} and mirror symmetries \hat{M}_x and \hat{M}_y . On the other hand, the remaining three types of square lattices are less symmetric, and the corner states split into two sets of twofold-degenerate pairs, as demonstrated in Fig. 11(a) for the example of a type-A square lattice with an even N_y . Their spatial distributions are illustrated in Figs. 11(b)–11(d), which reflects the \hat{M}_x , \hat{I} , and \hat{M}_y symmetries of the corresponding square structures, respectively.

In Fig. 12(a), we demonstrate the energy spectrum as a function of μ for a type-A square lattice with odd N_y , namely with both X - M and M - X zigzag edges. Each state is marked by a quantity Q defined to distinguish armchair and zigzag edge states,

$$Q = (\text{IPR})^{\frac{4}{5}} \times (\text{IPR}_x)^{\frac{1}{5}},$$

$$\text{IPR} = \sum_i \left[\sum_{\alpha} (|\psi_{i,\alpha,n}^{1st}|^2 + |\psi_{i,\alpha,n}^{2nd}|^2) \right]^2,$$

$$\text{IPR}_y = \sum_{i_y} \left[\sum_{\alpha, i_x} (|\psi_{i,\alpha,n}^{1st}|^2 + |\psi_{i,\alpha,n}^{2nd}|^2) \right]^2, \quad (\text{B1})$$

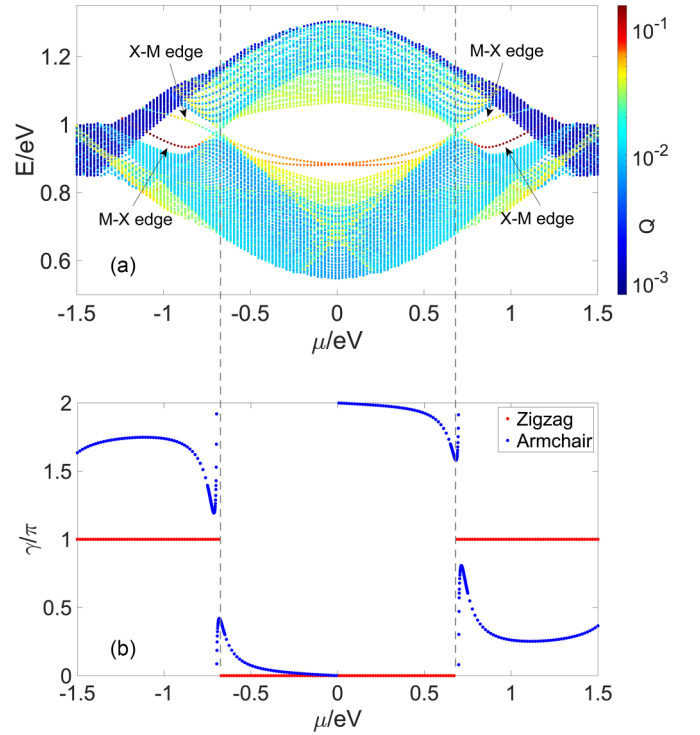


FIG. 12. (a) Eigenenergy vs on-site energy in AB-stacked bilayer TMDs with type-A structure and odd N_y . A total of 200 points around 0.92 eV are taken. The size of the lattice $N_x = 71, N_y = 71$. The interlayer coupling strength is chosen to be $\nu = 0.3$ eV. (b) Multiband Berry phases for all eigenstates below the edge gap, for zigzag (red) and armchair (blue) nanoribbons, respectively.

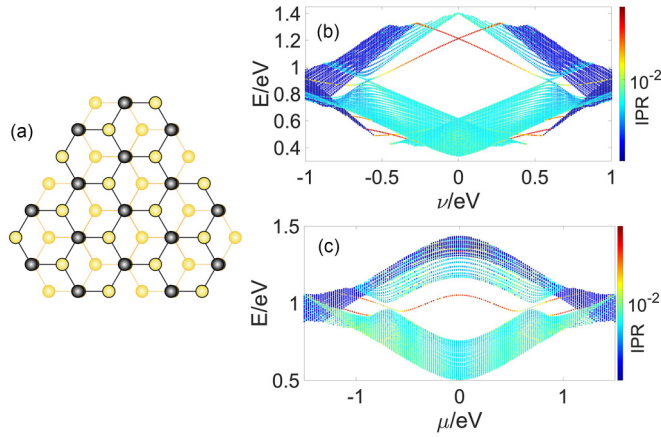


FIG. 13. Lattice structure and energy spectrum of triangular AB-stacked TMDs with armchair boundaries. (a) Top view of the triangular lattice with armchair boundaries. (b) Energy spectrum at $\mu = 0$ vs the interlayer hopping ν with 200 energy points around 0.85 eV. (c) Energy spectrum vs the layer-dependent on-site energy μ at $\nu = 0.3$ eV, with 200 energy points taken around 0.95 eV. The side length of the lattice is chosen to be $85 M$ atoms.

where the site index $i := (i_x, i_y)$ indicates different positions along the x and y directions, and IPR_y describes the localization strength along the y direction. With this definition, perfectly localized zigzag and armchair edge states are expected to have $Q \approx (1/N_x)^{4/5}$ and $1/N_y$, as they are localized along the y and x directions, respectively.

As shown in the figure, the fourfold-degenerate corner states split into two pairs of two-fold-degenerate ones, due to the breaking of inversion symmetry under a nonzero μ . The gap of both zigzag and armchair edge states closes at $|\mu| \approx 0.67$ eV, the same as for the cases with zigzag edges only. As discussed in the main text, the gap closing and reopening represents a topological phase transition that trivializes one of the M - X and X - M zigzag edges, thus only one pair of edge states can be attributed to zigzag edges when $|\mu| \gtrsim 0.67$ eV. However, the gap closing and reopening also indicate a band inversion for the armchair edge bands, which are gapped at $\mu = 0$. Thus we still observe two pairs of edge states after the transition, with one of them originating from an armchair-edge band inversion [at X - M edge for positive μ and M - X edge of negative μ ; see Fig. 12(a)].

In Fig. 12(b), we display the Berry phases of both zigzag and armchair nanoribbons, where the latter is found to be not quantized generally. Nevertheless, the armchair Berry phase is found to be 0 at $\mu = 0$, indicating that the armchair edges are topologically trivial when μ is small, i.e., within the parameter region between the two gap closing points for armchair edge states. The rapid change of the armchair Berry phase at the gap closing points suggests a transition analogous to a topological one, which reflects the origin of armchair-edge band inversion for one pair of edge states at $|\mu| \gtrsim 0.67$ eV.

Finally, we give a brief discussion of the quantization/nonquantization of these Berry phases. It is known that inversion symmetry can protect nontrivial topological insulating phases in 1D systems [48,49]. Taking the boundaries of the bilayer TMDs as 1D models, we note

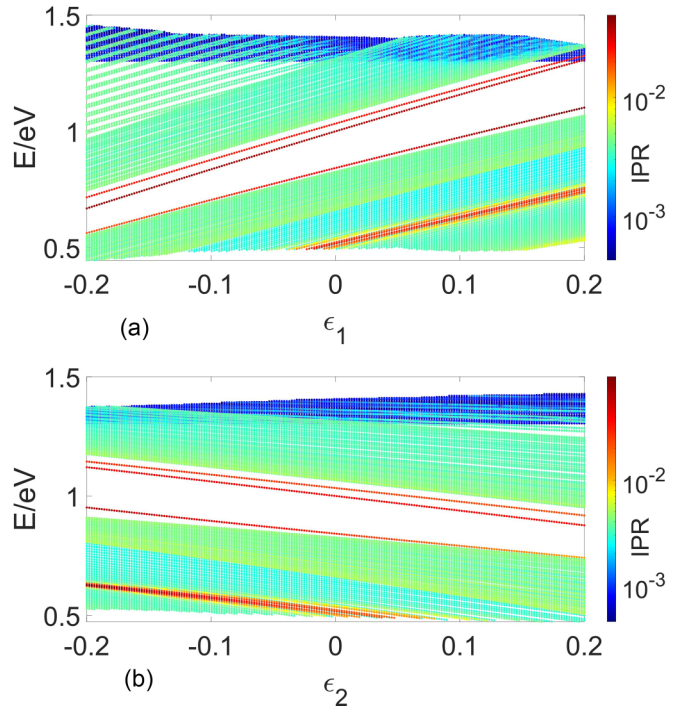


FIG. 14. Energy spectrum vs boundary perturbations for the AB-stacked TMDs with a parallelogram lattice. The size of the lattice is $N_x = 70, N_y = 70$. The interlayer hopping strength is chosen to be $\nu = 0.3$ eV. (a) Boundary perturbation on on-site energies, where edge parameters are $(1 + \epsilon_1)$ times of bulk ones. (b) Boundary perturbation on hopping strengths, where edge parameters are $(1 + \epsilon_2)$ times of bulk ones. A total of 300 energy points around 0.95 eV are taken for each panel.

that zigzag edges always satisfy an x -inversion symmetry (\hat{M}_x), but armchair edges satisfy a combining symmetry of y -inversion and layer exchange operations ($\sigma_x \hat{M}_y$) only at $\mu = 0$. Consistently, the zigzag Berry phase is always quantized, and the armchair one is quantized (zero) only in the absence of the energy detuning μ .

APPENDIX C: CORNER STATES OF ARMCHAIR BOUNDARIES

To confirm the origin of armchair-edge band inversion for edge states at $|\mu| \gtrsim 0.67$ eV, as discussed in Appendix B, we consider AB-stacked TMDs in a triangular structure with only armchair boundaries, as sketched in Fig. 13(a). Recent research has unveiled the existence of crystalline symmetry-protected corner states in a triangular monolayer of TMDs with armchair edges [24]. Hence, there are sixfold-degenerate corner states in our bilayer system when $\nu = 0$ and $\mu = 0$ (decoupled monolayers with no energy detuning). Upon turning on interlayer hopping ν , the corner states split into two sets of threefold-degenerate ones, as shown in Fig. 13(b).

In Fig. 13(c), we display the spectrum versus the energy detuning μ at $\nu = 0.3$ eV, i.e., the same as in Fig. 12. For $|\mu| \lesssim 0.67$ eV, only one set of the crystalline-symmetry-protected threefold-degenerate corner states can be found in the gap, as the other one merges into edge/bulk bands at $\nu = 0.3$ eV [see Fig. 13(b)]. Two sets of threefold-degenerate corner states

are seen to emerge when $|\mu|$ exceeds 0.67 eV, where the armchair-edge gap closes and the Berry phase in Fig. 12(b) jumps rapidly, confirming the origin of armchair-edge band inversion for corner states of the square lattice at large $|\mu|$ [Fig. 12(a)].

APPENDIX D: STABILITY OF CORNER STATES AGAINST BOUNDARY PERTURBATION

Natural solid systems are often affected by boundary effects, such as couplings to the environment or adjacent

systems, which may induce a difference between bulk and edge parameters. To confirm the stability of topological corner states in our model, we display numerical results of the energy spectrum for a parallelogram lattice with different boundary perturbations in Fig. 14. In particular, we take boundary on-site energies and hopping strengths to be $(1 + \epsilon_1)$ and $(1 + \epsilon_2)$ times those of bulk parameters, as demonstrated in Figs. 14(a) and 14(b), respectively. It is seen that the energy gap and in-gap corner states (shown in red with larger IPR) are robust against perturbations up to 20% of bulk parameters, which verifies the stability of the higher-order topological phases in our model.

-
- [1] M. Z. Hasan and C. L. Kane, *Colloquium: Topological insulators*, *Rev. Mod. Phys.* **82**, 3045 (2010).
- [2] X.-L. Qi and S.-C. Zhang, *Topological insulators and superconductors*, *Rev. Mod. Phys.* **83**, 1057 (2011).
- [3] W. A. Benalcazar, B. A. Bernevig, and T. L. Hughes, *Electric multipole moments, topological multipole moment pumping, and chiral hinge states in crystalline insulators*, *Phys. Rev. B* **96**, 245115 (2017).
- [4] W. A. Benalcazar, B. A. Bernevig, and T. L. Hughes, *Quantized electric multipole insulators*, *Science* **357**, 61 (2017).
- [5] F. Schindler, A. M. Cook, M. G. Vergniory, Z. Wang, S. S. P. Parkin, B. A. Bernevig, and T. Neupert, *Higher-order topological insulators*, *Sci. Adv.* **4**, eaat0346 (2018).
- [6] F. Schindler, Z. Wang, M. G. Vergniory, A. M. Cook, A. Murani, S. Sengupta, A. Y. Kasumov, R. Deblock, S. Jeon, I. Drozdov, H. Bouchiat, S. Guéron, A. Yazdani, B. A. Bernevig, and T. Neupert, *Higher-order topology in bismuth*, *Nat. Phys.* **14**, 918 (2018).
- [7] M. J. Park, Y. Kim, G. Y. Cho, and S. Lee, *Higher-order topological insulator in twisted bilayer graphene*, *Phys. Rev. Lett.* **123**, 216803 (2019).
- [8] Y. Fang and J. Cano, *Higher-order topological insulators in antiperovskites*, *Phys. Rev. B* **101**, 245110 (2020).
- [9] A. Agarwala, V. Juričić, and B. Roy, *Higher-order topological insulators in amorphous solids*, *Phys. Rev. Res.* **2**, 012067(R) (2020).
- [10] B.-Y. Xie, G.-X. Su, H.-F. Wang, H. Su, X.-P. Shen, P. Zhan, M.-H. Lu, Z.-L. Wang, and Y.-F. Chen, *Visualization of higher-order topological insulating phases in two-dimensional dielectric photonic crystals*, *Phys. Rev. Lett.* **122**, 233903 (2019).
- [11] Q. Wei, X. Zhang, W. Deng, J. Lu, X. Huang, M. Yan, G. Chen, Z. Liu, and S. Jia, *Higher-order topological semimetal in acoustic crystals*, *Nat. Mater.* **20**, 812 (2021).
- [12] H. Xue, Y. Yang, F. Gao, Y. Chong, and B. Zhang, *Acoustic higher-order topological insulator on a kagome lattice*, *Nat. Mater.* **18**, 108 (2019).
- [13] X. Ni, M. Weiner, A. Alù, and A. B. Khanikaev, *Observation of higher-order topological acoustic states protected by generalized chiral symmetry*, *Nat. Mater.* **18**, 113 (2019).
- [14] Z.-Z. Yang, X. Li, Y.-Y. Peng, X.-Y. Zou, and J.-C. Cheng, *Helical higher-order topological states in an acoustic crystalline insulator*, *Phys. Rev. Lett.* **125**, 255502 (2020).
- [15] H. Fan, B. Xia, L. Tong, S. Zheng, and D. Yu, *Elastic higher-order topological insulator with topologically protected corner states*, *Phys. Rev. Lett.* **122**, 204301 (2019).
- [16] B. Xie, H.-X. Wang, X. Zhang, P. Zhan, J.-H. Jiang, M. Lu, and Y. Chen, *Higher-order band topology*, *Nat. Rev. Phys.* **3**, 520 (2021).
- [17] B. A. Bernevig, C. Felser, and H. Beidenkopf, *Progress and prospects in magnetic topological materials*, *Nature (London)* **603**, 41 (2022).
- [18] B. J. Wieder, B. Bradlyn, J. Cano, Z. Wang, M. G. Vergniory, L. Elcoro, A. A. Soluyanov, C. Felser, T. Neupert, N. Regnault *et al.*, *Topological materials discovery from crystal symmetry*, *Nat. Rev. Mater.* **7**, 196 (2022).
- [19] H. Rostami, R. Asgari, and F. Guinea, *Edge modes in zigzag and armchair ribbons of monolayer MoS₂*, *J. Phys.: Condens. Matter* **28**, 495001 (2016).
- [20] J. R. Durán Retamal, D. Periyangounder, J.-J. Ke, M.-L. Tsai, and J.-H. He, *Charge carrier injection and transport engineering in two-dimensional transition metal dichalcogenides*, *Chem. Sci.* **9**, 7727 (2018).
- [21] M. Pandey, F. A. Rasmussen, K. Kuhar, T. Olsen, K. W. Jacobsen, and K. S. Thygesen, *Defect-tolerant monolayer transition metal dichalcogenides*, *Nano Lett.* **16**, 2234 (2016).
- [22] R. Wu, Q. Tao, W. Dang, Y. Liu, Bo Li, J. Li, B. Zhao, Z. Zhang, H. Ma, G. Sun, X. Duan, and X. Duan, *van der Waals epitaxial growth of atomically thin 2D metals on dangling-bond-free WSe₂ and WS₂*, *Adv. Funct. Mater.* **29**, 1806611 (2019).
- [23] Z. Wang, B. J. Wieder, J. Li, B. Yan, and B. A. Bernevig, *Higher-order topology, monopole nodal lines, and the origin of large fermi arcs in transition metal dichalcogenides XTe₂ (X = Mo, W)*, *Phys. Rev. Lett.* **123**, 186401 (2019).
- [24] J. Zeng, H. Liu, H. Jiang, Q.-F. Sun, and X. C. Xie, *Multiorbital model reveals a second-order topological insulator in 1H transition metal dichalcogenides*, *Phys. Rev. B* **104**, L161108 (2021).
- [25] S. Qian, G.-B. Liu, C.-C. Liu, and Y. Yao, *C_n-symmetric higher-order topological crystalline insulators in atomically thin transition metal dichalcogenides*, *Phys. Rev. B* **105**, 045417 (2022).
- [26] J. Jung and Y.-H. Kim, *Hidden breathing kagome topology in hexagonal transition metal dichalcogenides*, *Phys. Rev. B* **105**, 085138 (2022).
- [27] M. Costa, B. Focassio, L. M. Canonico, T. P. Cysne, G. R. Schleder, R. B. Muniz, A. Fazzio, and T. G. Rappoport, *Connecting higher-order topology with the orbital Hall effect in*

- monolayers of transition metal dichalcogenides, *Phys. Rev. Lett.* **130**, 116204 (2023).
- [28] G.-B. Liu, W.-Y. Shan, Y. Yao, W. Yao, and Di Xiao, Three-band tight-binding model for monolayers of group-VIB transition metal dichalcogenides, *Phys. Rev. B* **88**, 085433 (2013).
- [29] H. Pan, M. Xie, F. Wu, and S. Das Sarma, Topological phases in ab-stacked MoTe₂/WSe₂: \mathbb{Z}_2 topological insulators, Chern insulators, and topological charge density waves, *Phys. Rev. Lett.* **129**, 056804 (2022).
- [30] M. Geier, L. Trifunovic, M. Hoskam, and P. W. Brouwer, Second-order topological insulators and superconductors with an order-two crystalline symmetry, *Phys. Rev. B* **97**, 205135 (2018).
- [31] L. Trifunovic and P. W. Brouwer, Higher-order bulk-boundary correspondence for topological crystalline phases, *Phys. Rev. X* **9**, 011012 (2019).
- [32] M. Ezawa, Edge-corner correspondence: Boundary-obstructed topological phases with chiral symmetry, *Phys. Rev. B* **102**, 121405(R) (2020).
- [33] K. Asaga and T. Fukui, Boundary-obstructed topological phases of a massive Dirac fermion in a magnetic field, *Phys. Rev. B* **102**, 155102 (2020).
- [34] X. Wu, W. A. Benalcazar, Y. Li, R. Thomale, C.-X. Liu, and J. Hu, Boundary-obstructed topological high- T_c superconductivity in iron pnictides, *Phys. Rev. X* **10**, 041014 (2020).
- [35] A. Tiwari, A. Jahin, and Y. Wang, Chiral Dirac superconductors: Second-order and boundary-obstructed topology, *Phys. Rev. Res.* **2**, 043300 (2020).
- [36] E. Khalaf, W. A. Benalcazar, T. L. Hughes, and R. Queiroz, Boundary-obstructed topological phases, *Phys. Rev. Res.* **3**, 013239 (2021).
- [37] L. Li, M. Umer, and J. Gong, Direct prediction of corner state configurations from edge winding numbers in two- and three-dimensional chiral-symmetric lattice systems, *Phys. Rev. B* **98**, 205422 (2018).
- [38] L. Li, W. Zhu, and J. Gong, Direct dynamical characterization of higher-order topological phases with nested band inversion surfaces, *Sci. Bull.* **66**, 1502 (2021).
- [39] Z. Lei, Y. Deng, and L. Li, Topological classification of higher-order topological phases with nested band inversion surfaces, *Phys. Rev. B* **106**, 245105 (2022).
- [40] L. Li, E. V. Castro, and P. D. Sacramento, Strain-induced topological phase transition at zigzag edges of monolayer transition-metal dichalcogenides, *Phys. Rev. B* **94**, 195419 (2016).
- [41] T. Čadež, L. Li, E. V. Castro, and J. M. P. Carmelo, Robust one dimensionality at twin grain boundaries in MoSe₂, *Phys. Rev. B* **99**, 155109 (2019).
- [42] F. M. Brito, L. Li, J. M. V. P. Lopes, and E. V. Castro, Edge magnetism in transition metal dichalcogenide nanoribbons: Mean field theory and determinant quantum Monte Carlo, *Phys. Rev. B* **105**, 195130 (2022).
- [43] A. Ramasubramanian, D. Naveh, and E. Towe, Tunable band gaps in bilayer transition-metal dichalcogenides, *Phys. Rev. B* **84**, 205325 (2011).
- [44] A. Kumar and P. K. Ahluwalia, Semiconductor to metal transition in bilayer transition metal dichalcogenides MX₂ ($M = \text{Mo, W}$; $X = \text{S, Se, Te}$), *Modell. Simul. Mater. Sci. Eng.* **21**, 065015 (2013).
- [45] J. C. Slater and G. F. Koster, Simplified LCAO method for the periodic potential problem, *Phys. Rev.* **94**, 1498 (1954).
- [46] H. H. Jaffé, Some overlap integrals involving d orbitals, *J. Chem. Phys.* **21**, 258 (1953).
- [47] J. L. Roberts and H. H. Jaffé, Some overlap integrals involving d orbitals. II, *J. Chem. Phys.* **27**, 883 (1957).
- [48] F. Pollmann and A. M. Turner, Detection of symmetry-protected topological phases in one dimension, *Phys. Rev. B* **86**, 125441 (2012).
- [49] H. Guo and S. Chen, Kaleidoscope of symmetry-protected topological phases in one-dimensional periodically modulated lattices, *Phys. Rev. B* **91**, 041402(R) (2015).